Journal of MATERIALS RESEARCH

Invited Feature Paper
DOI: 10.1557/s43578-020-00068-3

EARLY CAREER SCHOLARS IN MATERIALS SCIENCE

ANNUAL ISSUE

Accelerated microwave-assisted synthesis and in situ X-ray scattering of tungsten-substituted vanadium dioxide ($V_{1-x}W_xO_2$)

Catrina E. Wilson[1,2,b], Amanda E. Gibson[1,2,b], Joshua J. Argo[1,2], Patricia A. Loughney[1,2], Wenqian Xu[3], Graham King[4], Vicky Doan-Nguyen[1,2,5,a]

[1]Department of Materials Science and Engineering, The Ohio State University, Columbus, Ohio 43212, USA
[2]Center for Electron Microscopy and Analysis, The Ohio State University, Columbus, Ohio 43212, USA
[3]X-ray Science Division, Advanced Photon Source, Argonne National Laboratory, Lemont, Illinois 60439, USA
[4]Brockhouse Beamlines, Canadian Light Source, Saskatoon, Saskatchewan S7N 2V3, Canada
[5]Department of Mechanical and Aerospace Engineering, The Ohio State University, Columbus, Ohio 43210, USA
[a)]Address all correspondence to this author. e-mail: doan-nguyen.1@osu.edu
[b)] These authors contributed equally to this work.

Received: 29 May 2020; accepted: 25 August 2020; published online: 4 February 2021

Vanadium dioxide (VO_2) has been widely studied due to its metal-insulator phase transition at 68 °C, below which it is a semiconducting monoclinic phase, $P2_1/c$, and above it is a metallic tetragonal phase, $P4_2/mnm$. Substituting vanadium with transition metals allows transition temperature tunability. An accelerated microwave-assisted synthesis for VO_2 and *5d* tungsten-substituted VO_2 presented herein decreased synthesis time by three orders of magnitude while maintaining phase purity, particle size, and transition character. Tungsten substitution amount was determined using inductively coupled plasma-optical emission spectroscopy. Differential scanning calorimetry, superconducting quantum interference device measurements, and *in situ* heating and cooling experiments monitored through synchrotron X-ray diffraction (XRD) confirmed the transition temperature decreased with increased tungsten substitution. Scanning electron microscopy analyzed through the line-intercept method produced an average particle size of 3–5 μm. Average structure and local structure phase purity was determined through the Rietveld analysis of synchrotron XRD and the least-squares refinement of pair distribution function data.

Prof. Doan-Nguyen is an Assistant Professor in the Departments of Materials Science & Engineering and Mechanical & Aerospace Engineering. She joined OSU in August 2017 as part of the Discovery Themes' Materials and Manufacturing for Sustainability Initiative. As a faculty affiliate of OSU's Center for Electron Microscopy and Analysis (CEMAS), her cross-cutting research includes synthesis, *in-situ* structural characterization, and functional testing of smart materials as well as advanced materials for energy storage and conversion. Before joining OSU, she was a UC President's Postdoctoral and Elings Prize Fellow at the University of California, Santa Barbara. She received her Ph.D. in Materials Science and Engineering at the University of Pennsylvania and B.S. in Chemistry and Women's and Gender Studies at Yale University. She has been recognized by the American Physical Society with the Stanford Ovshinsky Sustainable Energy Fellowship, the American Crystallographic Association with the Margaret C. Etter Lecturer Award and the Oak Ridge Associated Universities Ralph E. Power Junior Faculty Enhancement Award. Prof. Doan-Nguyen is also spearheading and contributing to projects on development of K-12 STEM education in the Columbus area and beyond.

Introduction

The semiconducting to metal phase transition (MIT) of vanadium dioxide (VO_2) has been extensively studied since it was first reported by Morin in 1959 [1]. The mechanism of the first-order transition [2, 3, 4] has been debated by many scholars over the years and has been primarily centered around electronic origins [4, 5, 6, 7, 8]. At $T < 68$ °C, the structure is monoclinic $P2_1/c$ (M1), and $T > 68$ °C, it is rutile tetragonal $P4_2/mnm$ (R)

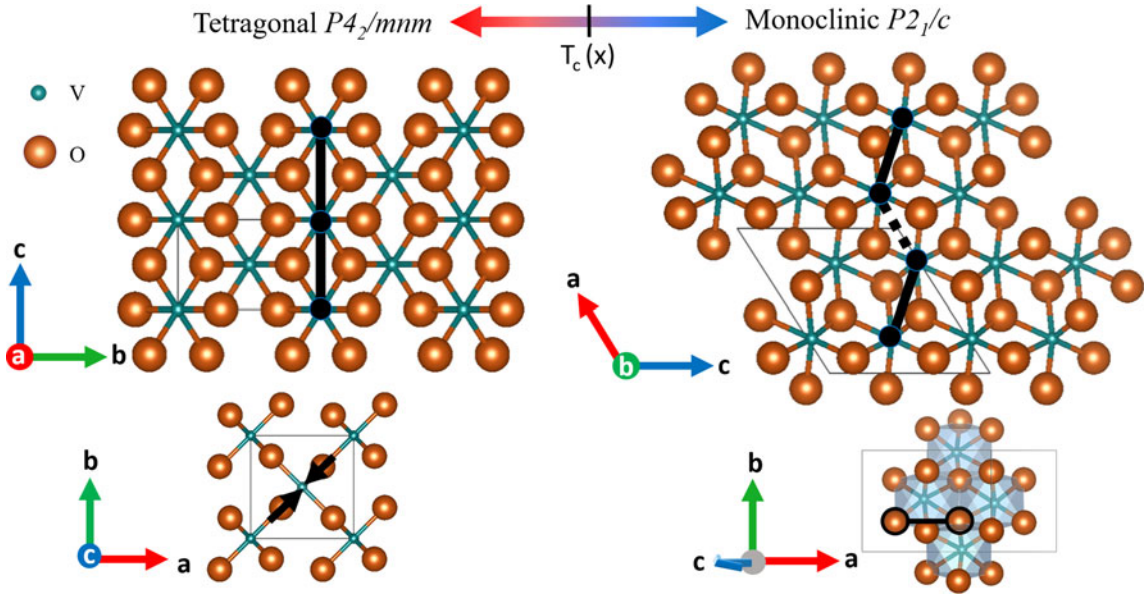

Figure 1: Crystallographic representations of both phases illustrating the dimerization of the V–V bonds caused by a decrease in distance between the O–O on the basal plane with cooling, shown on bottom left. The resulting O–O inter-octahedron overlap is highlighted in the monoclinic structure on the bottom right.

[9, 10, 11, 12]. The material sees a large increase in electronic conductivity, an increase in paramagnetic susceptibility, and a change in optical properties from IR-transparent to IR-reflective upon heating beyond the critical transition temperature [2, 13, 14, 15, 16, 17, 18, 19]. The M1 to R transition is marked by the increasing in V–V interatomic distances and a zigzag to linear arrangement [9, 10, 11, 20], as can be seen in Fig. 1.

Mechanism of the metal-insulator transition

The argument for a Mott–Hubbard transition has been supported by magnetic and electrical measurements, attributing the transition to strong electron–electron correlations due to temperature changes [11, 21, 22]. Conversely, a Peierls transition has been suggested as a result of an unstable Fermi surface due to electron–phonon interactions, triggering dimerization of atoms along the V–V chain [7, 8, 23]. More recently, a mixed Mott–Peierls model has been advocated to explain the transition [17].

Additionally, a purely structural explanation has been proposed to explain certain phenomena, such as intermediate monoclinic phases, i.e., *C2/m* (M2/B), that appear with Ti and Cr substitution, and is otherwise not addressed in the preceding arguments [3, 7, 24]. In a detailed review of rutile metal oxide compounds with an emphasis on the implications for the VO_2 MIT, Hiroi accounts the transition to inherent structural instabilities in the lattice [24]. The transition is characterized by a decrease in the *c/a* ratio of lattice parameters upon cooling through the transition temperature. As *c/a* decreases, covalent O–O bonds of the basal plane perpendicular to the *c*-axis break and accommodate the dimerized V–V bonding characteristic of the monoclinic phase [24]. The crystal structure of each phase is illustrated in Fig. 1 to show the dimerization of the V atoms in the monoclinic phase and the changing of positions of the accommodating O–O bonds. Hiroi further proposes that the difference in energy of the split $d_{//}$ orbitals, as the d_{xz} and d_{yz} orbitals split from the $d_x2_{-y}2$ orbital to form a π^* band, between the two phases can be explained by electron–electron correlations caused by the structural transition, as neither the structural transition nor the correlations alone account for this value [3, 22].

Furthermore, substitution studies with 3*d*, 4*d*, and 5*d* cations support that the transition is related to the structural instability rather than electronic interactions [24, 25, 26]. Specifically, in $Ti_xV_{1-x}O_2$, upon high substitution amounts of titanium, there is a relatively small impact on the MIT temperature in comparison to other substituents [24]. Titanium would be contributing many holes to the electronic system at high substitution amounts, encouraging an electronic transition to occur if electron correlations were the phase transformation mechanism. However, this is not observed given the small change in the MIT temperature upon substitution up to 20 at.% titanium [24]. Furthermore, substitutions involving larger atoms like tungsten (W) show strong depression of the MIT temperature [19, 25, 26, 27, 28, 29, 30], suggesting increased instability in the lattice accompanied by these substitutions.

Applications and contemporary synthesis methods

The relatively low transition temperature and the tunability *via* substitution atoms make VO_2 and $V_{1-x}M_xO_2$ (M = Cr [11, 20, 21, 31], Ti [24], Al [32], Fe [24, 33], Nb [24, 34], Mo [14, 19,

27, 30], and W [19, 25, 26, 27, 28, 29, 30]) attractive materials for a variety of applications, such as sensors, actuators, thermal relays, memory devices, and thermochromic optical switching devices [35, 36]. Many of these applications utilize thin film and nanocrystalline morphologies, yet bulk powder has been considered a promising heat storage material [37] in addition to being used for structural studies [12, 38]. Reported bulk syntheses include sol–gel [39] and solid-state methodologies, both requiring days of high-temperature annealing and inert atmosphere [12, 14, 24, 33]. Extended synthesis time limits industrial applicability, demanding an alternative production route. Substitution homogeneity is also important for these applications as phase segregation leads to a loss in the sharp transition and poor characterization of property changes associated with the phase transformation [36].

Regarding morphology, nanoparticle applications are beginning to be imagined as new properties associated with quantum confinement have been recently discovered [36]. VO_2 nanoparticles have been grown with various morphologies *via* sol–gel approaches [35, 36], pulsed laser deposition (PLD) [35, 36], hydrothermal synthesis [19], and controlled reduction reaction [40]. Microwave-assisted heating has also been used to produce nanostructured VO_2 *via* solvothermal synthesis [41, 42]. Radio frequency (RF) sputtering [43], metal-organic chemical vapor deposition (MOCVD) [44], and PLD [32] methodologies have also been implemented to achieve nanometer-thick films. However, there are still many opportunities for the development of thin film and nanocrystalline microwave-assisted VO_2 syntheses to decrease the overall cost.

Microwave-assisted heating of solids

Microwave-assisted heating has been demonstrated for the accelerated production of a library of materials used in energy storage [45, 46], solid-state lighting [47], magnetocaloric refrigeration [48], heterogeneous catalysis [49], and peptide assembly [50, 51]. Several other metal oxides have also been shown to be viable systems for microwave-assisted solid-state syntheses [46, 52, 53, 54, 55, 56, 57, 58, 59, 60]. Microwave heating offers significant advantages over traditional furnaces due to the direct heating of materials *via* dielectric loss associated with dipolar and space-charge polarization, as well as DC conductivity, in an alternating electric field [46, 59, 60, 61]. For materials that do not contain water or another absorbed polar molecule, the latter two mechanisms will dominate [61].

Carbon was used as a susceptor in this synthesis for providing both consistent heating around the sample and to assist the precursors in reaching temperatures at which their dielectric properties may be more favorable for microwave heating. Susceptors are materials that readily convert electromagnetic energy to heat and can elevate the temperature to provide more advantageous heating of precursors [59]. Given the low mass loading of the sample, the volume of the carbon-filled crucible, and temperature studies of the susceptor at the power levels and time used in this synthesis, most of the heating of this synthesis is likely due to the radiation from the susceptor. However, the dielectric properties of VO_2 and its precursors are important to consider for scaled reactions.

Dielectric properties dictate how a material behaves in the presence of microwave radiation, which can shed light on the otherwise convoluted "black box" character of microwave–matter interactions. The complex permittivity gives two important equations that determine the heating efficiency and uniformity seen in the process of microwave heating [61]. The loss tangent ($\tan\delta = \varepsilon''/\varepsilon'$) describes the ratio of energy lost as heat, ε'', to energy stored in a dielectric medium, ε'. Thus, high $\tan\delta$ values ensure more efficient heating. The penetration depth is the depth of microwave penetration into a material derived such that the energy of the wave is $1/e$ (~0.37) of its original energy at that depth, given in Eq. (1) below [62] where λ_0 is the wavelength. A low penetration depth indicates a limited response of a material to absorb and interact with the microwave radiation and can limit batch sizes for such a material.

$$D_p = \frac{\lambda_0}{2\pi(2\varepsilon')^{1/2}}\left\{\left[1+\left(\frac{\varepsilon''}{\varepsilon'}\right)^2\right]^{1/2}-1\right\}^{-1/2}. \quad (1)$$

Values for the loss tangent and penetration depth of VO_2 were estimated from data presented by Émond et al. using digitized versions of their Figure 14 for the $P2_1/c$ phase and Figure 16 for the $P4_2/mnm$ phase to discuss scalable microwave processability [63]. The extracted ϵ' and ϵ'' (calculated from the conductivity plot) for the low-temperature monoclinic phase at 20 °C at 2.5 GHz yielded a loss tangent value of 1.9 and a penetration depth of 946 μm, as calculated from Eq. (1). The ϵ' and ϵ'' for the tetragonal phase at 100 °C and 2.5 GHz yielded a loss tangent value of 10.2 and a penetration depth of 25 μm. As VO_2 crystallizes at high reaction temperatures [64], heating efficiency will increase due to the $P4_2/mnm$ phase, which has an extremely high loss tangent compared with the lower temperature $P2_1/c$ phase. The penetration depth of ~25 μm of tetragonal VO_2 is well above the average particle size of the precursors and products used in scaled solid-state synthesis; therefore, VO_2 would be a promising candidate for microwave processing on a larger scale.

In this paper, an accelerated microwave-assisted synthesis is presented that decreases the synthesis time from days to tens of minutes and demonstrates substitution homogeneity in bulk powder samples. This is the first reported reaction to produce bulk VO_2 (M1, $P2_1/c$) with microwave irradiation. Tungsten was selected as a substitution cation in this study because it causes the greatest depression of the MIT temperature and to

probe its effect on local structure stability [19, 25, 26, 27, 28, 29, 30]. The synthesis presented of bulk $P2_1/c$ VO_2 and W-substituted VO_2 involves a one-pot synthesis at 1080 W for 15 min, followed by 840 W for 30 min, for a total reaction time of 45 min. The characterization of the sample series was performed *via* inductively coupled plasma-optical emission spectroscopy (ICP-OES), X-ray diffraction (XRD) performed at room temperature and *in situ* heating and cooling, differential scanning calorimetry (DSC), scanning electron microscopy (SEM), and superconducting quantum interference device (SQUID). Rietveld refinements of the XRD data were performed to determine phase purity and average structure, while pair distribution functions (PDFs) were refined *via* least-squares fitting to elucidate local structure information. This is the first reported local structure PDF of bulk powder tungsten-substituted VO_2.

Results and Discussion

Elemental analysis of samples

ICP-OES was performed to quantitatively analyze the atomic percentages of tungsten substitution within VO_2 (Table 1). The substitution was kept below 10 at.% to avoid phase segregation given that the ionic radius of tungsten is 11% larger than that of vanadium when both are in the +4-oxidation state. Due to the sensitivity of ICP-OES to local inhomogeneities within the sample, a relatively large amount of sample (~50 mg) was digested and diluted to obtain an accurate representation of the bulk sample. The ICP-OES results indicate that the tungsten substitution was near the nominal substitution amount (0.2, 5, and 8 at.%) and phase segregation was most likely not occurring within the bulk. If phase segregation of W-rich or V-rich phases were occurring, the small amount provided for ICP-OES would give atomic percentages that vary greatly compared with nominal substitution amounts with little reproducibility of results across samples.

Determining phase purity using XRD

VO_2 can stabilize in a variety of polymorphs, and to ensure monoclinic phase purity, XRD was obtained and Rietveld analysis performed. Simulated powder diffraction patterns for other polymorphs of VO_2 that could have stabilized are presented in Supplementary Fig. S1. The Rietveld refinement of room temperature synchrotron powder XRD data indicates phase purity throughout the substitution series, as shown in Fig. 2. The low substitution samples ($x < 0.046$) were fit to the monoclinic $P2_1/c$ space group, and the high substitution phase ($x > 0.046$) was fit to the tetragonal $P4_2/mnm$ space group [3, 25, 26, 27]. The intermediate ($x = 0.046$) was fit to both the monoclinic and tetragonal space groups, producing phase fractions of 0.15(1) and 0.85(1), respectively. The patterns match previously reported refinements well, giving fit residuals less than 10% [9]. The tungsten and vanadium site occupancy from the Rietveld refinement, Supplementary Tables S1–S3, produced similar values given by ICP-OES with little other structural changes.

Upon substitution of greater amounts of tungsten, the MIT is depressed as seen in Fig. 6, and the structure transitions from monoclinic to tetragonal at room temperature. The phase transition can be clearly seen by tracking the (110) peak shift and the $(11\bar{1})$ disappearance, highlighted in Fig. 2(b), along with the disappearance of multiple other higher Q reflections. Tracking the (110) peak center as a function of tungsten substitution amount provides a linear relationship shown in Fig. 2(c). There is only a slight shift between the unsubstituted VO_2 and $V_{0.997}W_{0.003}O_2$ due to the low substitution amount. Then, the $V_{0.954}W_{0.046}O_2$ (110) peak is dominated by the $P4_2/mnm$ structure (0.85(1) = rutile phase fraction) giving it the same peak center as $V_{0.921}W_{0.079}O_2$. However, a linear regression gives $R^2 = 0.869$ with $Q = 1.961(3) - 0.0024(6)\ x$, in which x is the substitution amount in atomic percent and providing Q in units of $Å^{-1}$. A comparison of these fits to analogous furnace-annealed samples is presented in Supplementary Fig. S2 and illustrates that similar purity can be achieved through the accelerated microwave synthesis. Fit residuals are like those of the microwave-annealed samples in Fig. 2. Further comparison of the two synthesis methods on the crystallographic structure also shows very little difference among lattice parameters, atomic positions, and thermal displacement factors in Supplementary Tables S1–S6.

The lattice parameters (a, b, c, and β) and the unit cell volume as a function of substitution amount is monitored in Fig. 3, which provides trends throughout the phase transformation that agree with typical furnace-annealed samples [27], also confirmed in this report in Supplementary Fig. S2. There is a 0.36(2)% volume expansion upon tungsten substitution up to 4.6 at.% corresponding to an increase in a, b, c, and β until the MIT is depressed below room temperature and the sample is in the tetragonal phase. The lattice parameters increase due to an increase in cation radius (W = 66 pm > V = 58 pm, each in +4 oxidation state with a coordination number of 6) [65]; therefore, as substitution onto the vanadium site increases, the unit cell volume increases. Future studies will include greater substitution amounts to discuss the tetragonal lattice

Table 1: ICP-OES results showing the atomic percentage of tungsten incorporated during synthesis, the weight percent of vanadium and tungsten, and the tungsten to vanadium ratio.

Nominal W (at.%)	ICP-OES W (at.%)	W (wt%)	V (wt%)
0.2	0.259(7)	0.576(5)	61.321(7)
5.0	4.596(6)	12.044(6)	69.233(6)
8.0	7.877(5)	16.383(0)	53.092(7)

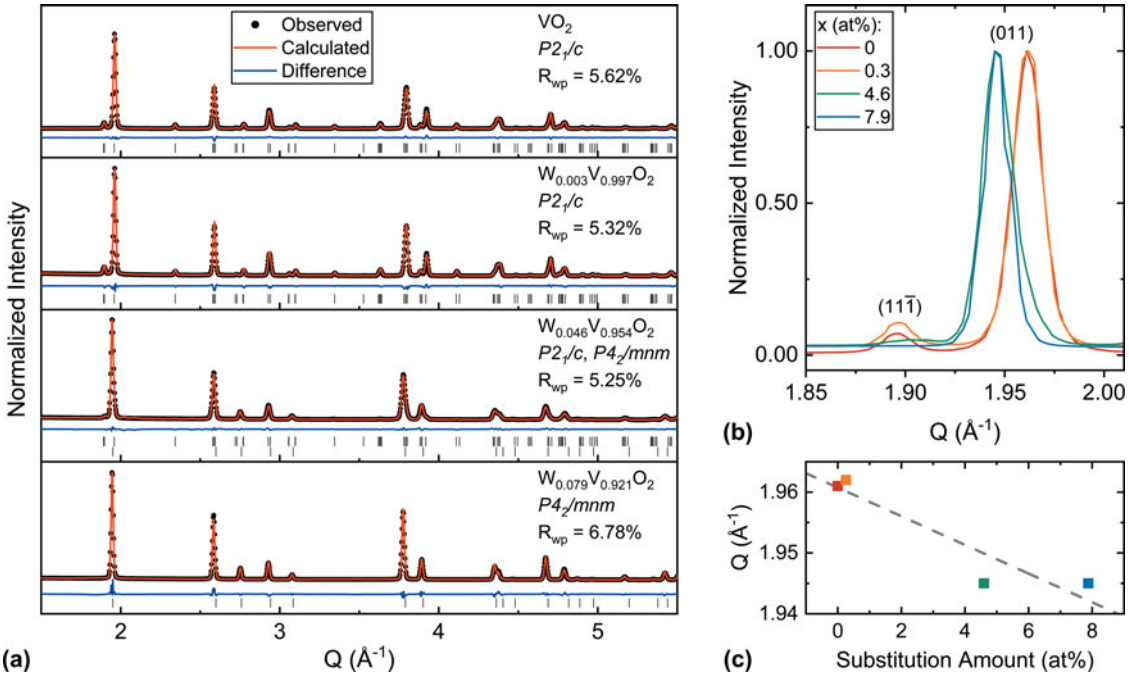

Figure 2: (a) Rietveld refinement (λ = 0.2399 Å for $x = 0$, and λ = 0.4133 Å for $x > 0$) using $P2_1/c$, and $P4_2/mnm$ along a substitution series ($0 < x < 0.079$) at room temperature illustrates phase purity with substitution. The phase associated with each fit is labeled on the top right corner of the plot, and phase markers are in gray at the bottom of the respective plot. (b) Tracking the (011) peak shift as the structure symmetrizes with increasing substitution amount. (c) Linear regression of the (011) peak center as a function of substitution amount producing fit results: $Q = 1.961(3) - 0.0024(6)x$, $R^2 = 0.869$.

parameter trends as has been done with $Mo_xV_{1-x}O_2$ systems [14, 27, 28].

As presented by Hiroi, the V–O octahedral distortion is dependent on the *c/a* ratio in the tetragonal structure [24]. As the tetragonal *c/a* ratio increases with increasing substitution amount, the oxygen anions along the *c*-axis are further separated, allowing for greater overlap along the [110] direction. This overlap is hypothesized to instigate covalent bonding between the overlapping oxide ions, driving the phase transformation. Therefore, as substitution increases, the *c/a* ratio increases, strengthening the O1–O2 inter-octahedra (O1 ∠ O2 = 94°) overlap, illustrated in Fig. 1, which inhibits direct V–V bond formation and decreases T_c.

In $P2_1/c$ structures, the *c/a* ratio of WO_2 and MoO_2 (0.58) is significantly lower (0.57) than that of the *c/a* ratio of the VO_2 (0.625); the difference of these ratios corresponds to the magnitude of MIT temperature depression that each cation substitution incurs in VO_2 [24]. This trend is also seen with TiO_2 and CrO_2, whose *c/a* ratios are larger and increase the transition temperature when cation-substituted into VO_2 [24]. This suggests that the substitution of these cations incurs a local *c/a* deviation into the structure that accelerates or retards the MIT temperature as a function of substitution amount. This hypothesis will be addressed in an upcoming report.

Using the lattice parameters from Rietveld refinement for the tetragonal samples, the *c/a* ratio increases by 0.135(5)% from 0.62814(3) to 0.62899(2) for 4.6–7.9 at.% substitution. This causes a dramatic change in the T_c measured through SQUID (Fig. 4). Where the 4.6 at.% sample demonstrated T_c = −93°C, but the 7.9 at.% T_c could not be captured throughout a temperature range of −263 to 77 °C.

Ex situ heating and cooling XRD measurements probed the structure on the other side of the phase transformation. This was achieved by heating the samples to 102 °C that were monoclinic at room temperature ($x < 0.046$) and cooling the samples to −183 °C that were tetragonal, or partially tetragonal at room temperature ($x > 0.005$). The data were also analyzed using Rietveld refinement and produced low residuals indicating a good fit to the expected phases, as shown in Fig. 4.

Local structure analysis using the PDF

The PDF provides the probability of finding two atoms separated by a distance, *r*. It is derived from the total scattering (Bragg and diffuse) structure function, $S(Q)$ which undergoes a Fourier transform to produce the PDF, $G(r)$, in Eq. (2) [66].

$$G(r) = \frac{2}{\pi}\int_0^{Q_{max}} Q[S(Q) - 1)]\sin(Qr)dQ. \quad (2)$$

Room temperature atomic PDF measurements analyzed through a least-squares refinement elucidated the local structure of VO_2 and $W_{0.002}V_{0.998}O_2$ (Fig. 5). The average structure of $W_{0.002}V_{0.998}O_2$ analyzed through Rietveld refinement is shown in Supplementary Fig. S3. The local structures fit well to the

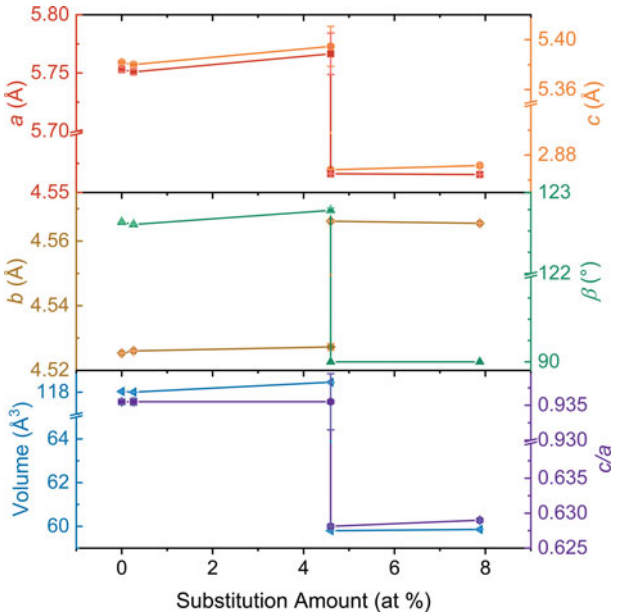

Figure 3: Lattice parameters (*a*, *b*, *c*, and β) and unit cell volume from Rietveld refinement tracked as a function of substitution amount show the same trends as furnace-annealed tungsten-substituted VO_2 samples [27].

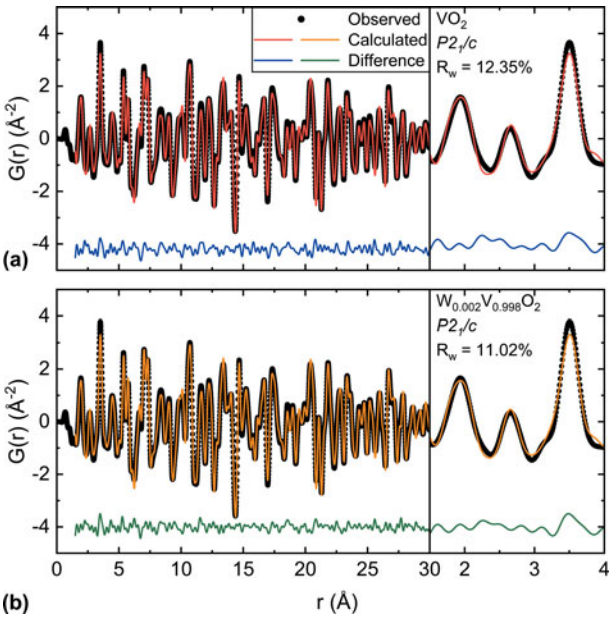

Figure 5: Experimental X-ray PDFs of **(a)** VO_2 and **(b)** $W_{0.002}V_{0.998}O_2$ both fit to $P2_1/c$ within a *r*-range of 1.5–30 Å.

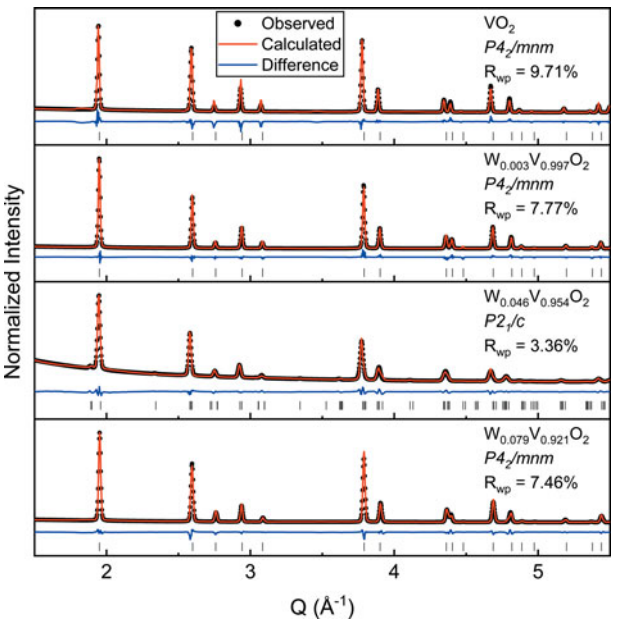

Figure 4: Rietveld refinement (λ = 0.4133 Å) performed using $P2_1/c$, and $P4_2/mnm$ at −183 °C for $x > 0.005$ and 102 °C for $x < 0.046$ indicates phase purity below and above the respective transition temperatures. An exception to this is $x = 0.079$, which is too highly substituted to reach $T_c = -183$ °C.

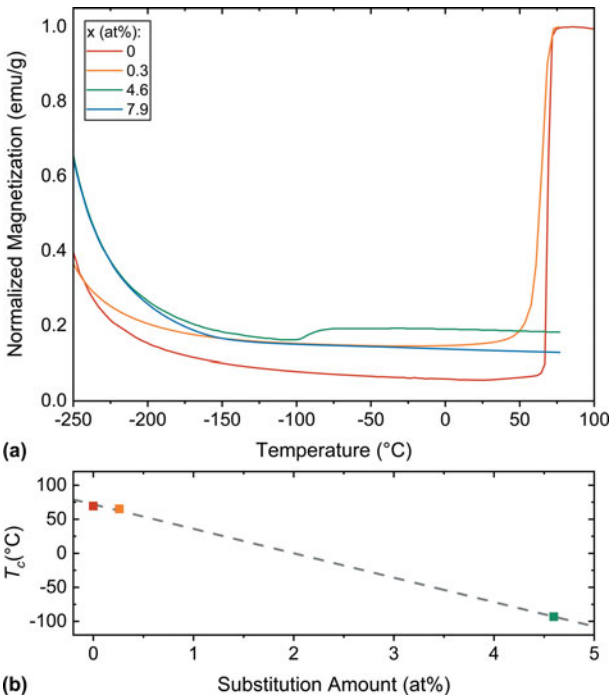

Figure 6: (a) Normalized magnetization from SQUID measurements of a substitution series of $W_xV_{1-x}O_2$. (b) Linear regression of transition temperature upon cooling as a function of substitution amount providing fit results: $T_c = 72(3) - 35(1)\,x$, $R^2 = 0.999$.

$P2_1/c$ space group in the *r*-range of 1.5–30 Å giving residuals of 12.35 and 11.02% for VO_2 and $W_{0.002}V_{0.998}O_2$, respectively. The nearest neighbor V–V distance is illustrated by the peak at 2.65 Å.

The *a*, *b*, and *c* lattice parameters increase by 0.06% from 0 to 0.2 at.% tungsten substitution. This was accompanied by a 4.65% decrease in U_{33}. Upon further substitution, it is expected that U_{33} will continue to decrease as the *c*/*a* ratio increases and there is less V–V dimerization along the *c*-axis leading to a shift of the 2.65 Å V–V peak. This has been demonstrated across a temperature series by Corr et al. [12]. However, this is the first

Table 2: Average grain sizes found for unsubstituted and highly substituted samples produced *via* traditional furnace annealing and accelerated microwave heating.

Nominal at.% W	Synthesis	Average grain size (μm)
0	Microwave	5.54
0	Furnace	4.06
8	Microwave	3.25
10	Furnace	4.95

reported instance of the local structure PDF of bulk powder tungsten-substituted VO_2.

Morphology and size comparison of synthesis methods

SEM images, in Supplementary Fig. S4, were acquired to ensure the accelerated synthesis did not perturb the bulk morphology compared with other synthesis techniques. The estimated grain sizes for the micrographs in Supplementary Fig. S4 were found using the linear-intercept method with the processed micrographs shown in Supplementary Fig. S5, and the values are presented in Table 2. The values for both highly substituted and unsubstituted samples produced *via* both furnace and microwave heating are similar amongst themselves and are on the same order of magnitude as previously reported values for bulk powder [30].

Measuring T_c through magnetic and structural characterization techniques

SQUID studies demonstrate Curie–Weiss paramagnetic behavior at low temperatures until the transition temperature (T_c) where there is a large jump but no discontinuity in paramagnetic susceptibility upon cooling correlated to a decrease in the resistivity [22, 38, 67]. The transition temperature ranges from −93.17 °C at 4.6 at.% tungsten substitution to 69.32 °C for the unsubstituted. The sharp decrease in magnetism without a discontinuity is typical of a first-order phase transformation, which is expected for this material [67]. The decreasing T_c is accompanied by a decrease in the difference of paramagnetic susceptibility between the monoclinic and tetragonal phase with increasing substitution amount until T_c is depressed enough that only the tetragonal phase is accessible. This is accompanied by an increasing Curie–Weiss contribution to the magnetization.

The T_c was obtained from SQUID by taking the derivative of the magnetization against the temperature and finding the maximum. T_c as a function of substitution amount illustrates a linear relationship between the transition temperature and substitution amount where the transition temperature depresses at a rate of −36.6 °C/at.% W, in Fig. 6. This is consistent with literature values of conventionally synthesized bulk substituted VO_2 [22, 29, 30, 67]. DSC results (Supplementary Fig. S6) for analogous samples corroborate the transition temperatures captured through SQUID measurements.

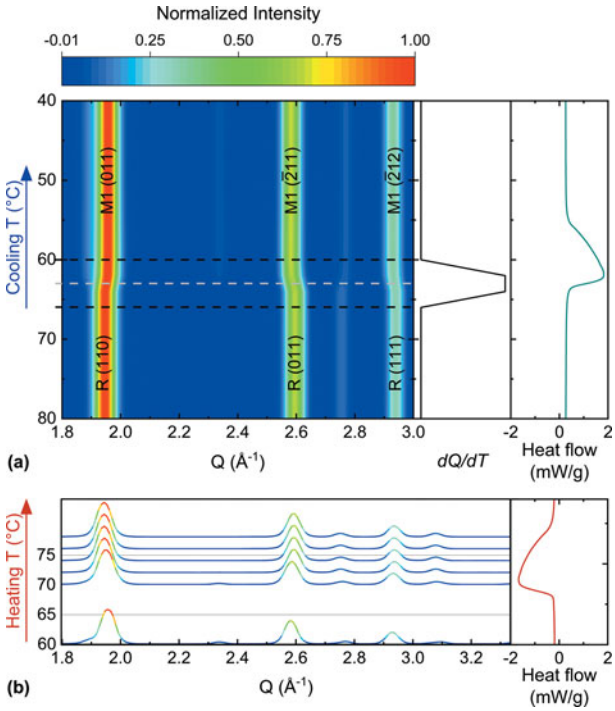

Figure 7: *In situ* heating (bottom pane) and cooling (top pane) while probing through synchrotron XRD (λ = 0.24162 Å) (a) waterfall plot upon cooling with the derivative of *Q* with respect to temperature and DSC indicating agreement of T_c across multiple techniques (b) stack plot of *I*(*q*) upon cooling illustrating the waterfall representation with DSC indicating T_c.

In situ heating and cooling experiments for an unsubstituted (Fig. 7) and 0.2 at.% tungsten-substituted (Fig. 8) sample were performed to monitor the structure throughout the phase transformation. The phase transition was tracked using the derivative of the (110) peak, which shifts from 1.956 to 1.947 $Å^{-1}$ when transitioning from monoclinic to tetragonal. The (*hkl*) planes represented were chosen because they are three of the highest intensity peaks for both the $P2_1/c$ and $P4_2/mnm$ bulk structures.

The unsubstituted VO_2 phase transformation upon heating is tracked by the disappearance of the $(10\bar{2})$ peak between 70 and 72 °C. This also agrees well with the DSC T_c (68 °C) and SQUID T_c (69 °C), which gives an idea of the range between the three techniques. Phase transformation reversibility is exemplified with the corresponding *in situ* cooling experiment.

The transition upon cooling occurred at a rate of $\Delta Q/\Delta T$ (−0.009 $Å^{-1}$/2 °C) within a range of 62–64 °C for the (110) peak. The transition temperature from *in-situ* cooling (63 °C) agrees with the DSC T_c upon cooling (62 °C) but is lower than SQUID T_c (69 °C). This illustrates the expected thermal hysteresis of the phase transition upon heating and cooling.

An *in situ* heating and cooling experiment was also performed for $W_{0.002}V_{0.998}O_2$, and the phase transition upon

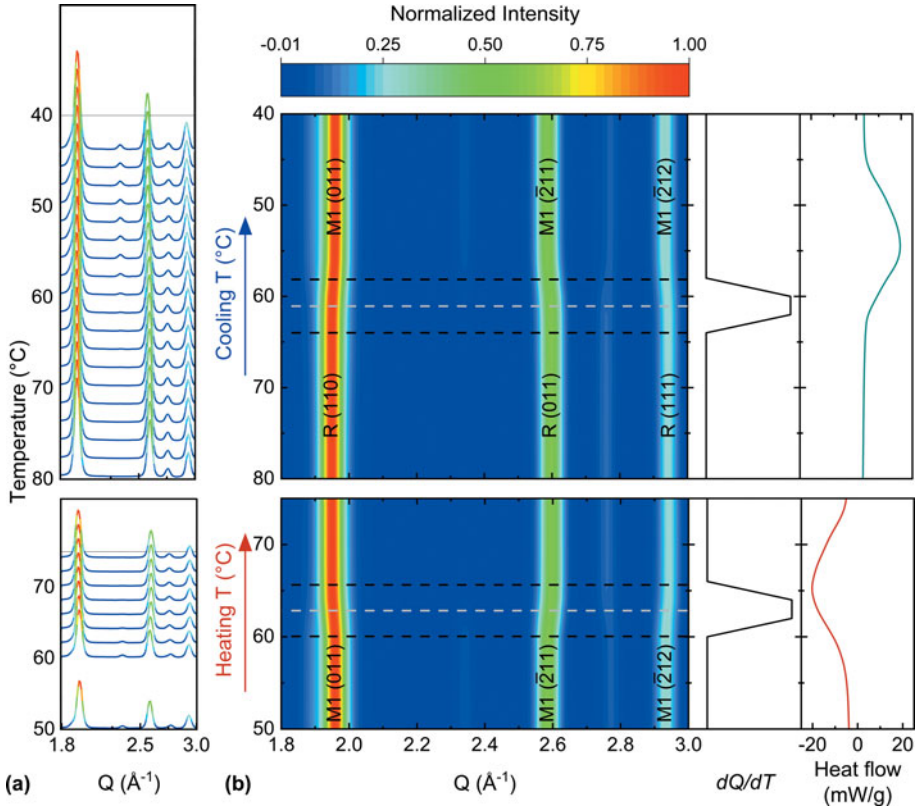

Figure 8: *In situ* heating (bottom pane) and cooling (top pane) while probing $W_{0.002}V_{0.998}O_2$ through synchrotron XRD ($\lambda = 0.24162$ Å) (a) stack plot representing (b) the waterfall plot with T_c determined from the derivative of Q with respect to temperature indicating agreement with DSC.

heating occurred over a temperature range of 60–66 °C corresponding to a rate of $\Delta Q/\Delta T$ (−0.009 $Å^{-1}$/6 °C). This rate is slightly larger than that of VO_2 due to the tungsten substitution [68]. The transition temperature from *in situ* heating (63 °C) aligns well with the DSC transition temperature (65 °C) and the transition temperature from the linear regression of the SQUID data (65 °C), like unsubstituted VO_2. As for the unsubstituted case, phase transformation reversibility was established with an *in situ* cooling experiment.

The phase transition upon cooling for $V_{0.998}W_{0.002}O_2$ occurred over a temperature range of 58–64 °C. This corresponds to a rate of $\Delta Q/\Delta T$ (−0.009 $Å^{-1}$/6 °C) upon cooling. The decreased T_c compared with VO_2 is expected from DSC and SQUID, which was 54 and 65 °C, respectively. The thermal hysteresis is also apparent in the substituted case. These transition temperatures agree with the *in situ* cooling experiment and lie within a range like that of the VO_2 measurements.

Conclusions

ICP-OES confirms that the nominal amount of tungsten incorporation is achieved through this microwave synthesis. Through the Rietveld refinement of synchrotron XRD data of these accelerated-synthesized microwave samples, a phase-pure product is attained. *Ex situ* XRD indicates that phase purity and structural integrity is maintained across the phase transformation. SEM illustrates that the particle size and morphology is comparable to other bulk synthetic approaches [30]. SQUID, DSC, and *in situ* heating and cooling XRD support a depression of the transition temperature with increasing tungsten substitution amount. The transition temperature from SQUID depresses at a rate of −36.6 °C/at.% W which is in line with the previous literature [3, 29, 30]. It can be concluded that the microwave-assisted synthesis decreases the synthesis time dramatically while maintaining the purity, morphology, and properties.

Methodology

V_2O_5 powder precursor (99% purity) was purchased from Sigma Millipore. Precursor phase purity was confirmed with XRD before use, shown in Supplementary Fig. S7. V_2O_3 was reduced from V_2O_5 in a 5% H_2/95% N_2 tube furnace at 800 °C for 24 h. Molar equivalents of V_2O_3 and V_2O_5 were ground together using agate mortar and pestle for 15 min before being placed in a 9 mm inner diameter fused silica tube. Approximately 330 mg of the mixed precursors were loaded into the ampoule as loose powder after initial experiments revealed significantly more advanced reactions for broken pellets than for intact pellets for identical heating settings. Ampules were sealed using conventional air-free Schlenk line techniques after being evacuated for 30 min to

control the oxygen pressure. Ampules were loaded into zirconia crucibles with 5 mm thick walls and a volume of approximately 87 cm^3 filled with approximately 90 g of coarse activated carbon microwave susceptor, as shown in Supplementary Fig. S8. Microwave-assisted heating experiments were carried out in a domestic multi-mode microwave oven (Panasonic (Kadoma, Japan) NN-SN651W) at a 1080 W for 15 min and then immediately followed by heating at 840 W for 30 min. This heating schedule was determined experimentally after an initial temperature study was performed by measuring the temperature of the carbon at various power outputs for selected time lengths. Small amounts of intermediate vanadium oxides were seen in XRD for experiments without the additional 30 min of annealing time. In this domestic microwave oven, one can choose a power level that corresponds to a percentage of the total power of the oven (1200 W), for example, power level 9 is 90% of 1200 W to yield 1080 W. The rotating plate was removed from the oven to prevent shattering due to extreme heat from the susceptor through the zirconia crucible. Before the ampules were placed into the crucible, the carbon was heated at 1080 W for 2 min to yield surface temperatures around 200 °C, measured with a Grainger Westward (Ontario, Canada) LCD infrared thermometer model # 54TZ30. Surface temperatures measured after the initial high-power step were measured at around 1000–1100°C and seen to be maintained after the 30-min annealing time. All products were air cooled within the carbon-filled crucible and ground again in agate mortar for 15 min.

The series of $V_{1-x}W_xO_2$ microwave-assisted heated samples were prepared by mixing powder reactants in evacuated, sealed ampoules. WO_2 (99.99% purity) from Sigma Millipore was used as the tungsten source and was mixed in stoichiometric ratios with the vanadium oxides to achieve target substitution amounts. These were then heated in a conventional microwave in the same manner described previously. Additional samples were produced *via* traditional heating in a model FD1545M Thermolyne muffle furnace from Thermo Scientific (Waltham, Massachusetts) at 1050 °C for 216 h (9 days); all other synthesis parameters were identical (Supplementary Fig. S2).

Ambient condition synchrotron XRD was collected at the Advanced Photon Source at Argonne National Laboratory (Lemont, Illinois) at beamline 17-BM. The *ex situ* heating and cooling XRD was collected at the Brockhouse Beamlines at the Canadian Light Source (Saskatchewan, Canada) at sector BXDS-WHE, 04 ID-01. Rietveld refinements of room temperature synchrotron XRD data were performed using GSAS-II [69]. Parameters that were refined included (i) lattice parameters, (ii) site occupancies for tungsten and vanadium, (iii) atomic displacement parameters with the cations held equivalent and the anions held equivalent, (iv) fractional atomic coordinates with tungsten and vanadium held equivalent, (v) peak shape, (vi) background Chebyshev coefficients of degree eight, and (vii) scale factor. Refinements utilized the following.-cif files for the $P2_1/c$ and $P4_2/mnm$ structures, respectively: ICSD-34033 and ICSD-1504.

The *in situ* heating and cooling experiments were also conducted at the Advanced Photon Source at Argonne National Laboratory at beamline 17-BM ($\lambda = 0.24162$ Å) using an Oxford Cryosystems (Long Hanborough, United Kingdom) Cryostream 700 Plus situated above the sample and resistive heaters around the capillary. The *in situ* experimental configuration is shown in Supplementary Fig. S9 without the Cryostream 700 Plus. When the Cryostream was used, the nozzle was positioned above and as close to the sample as possible without impeding data collection. The samples were packed in glass capillaries, and the ends plugged with quartz wool. This allowed helium flow over the sample to be used to prevent secondary phases from forming during heating/cooling. The samples were quickly heated (6 °C/min) to reach a temperature close to the phase transformation (T_c − 10 °C) where it was slowly heated (2 °C/min) through the phase transformation. The sample was then cooled in a symmetric fashion. The T_c was determined from SQUID and DSC data collected prior to these experiments (Supplementary Fig. S6).

ICP-OES was performed with a Perkin Elmer (Waltham, Massachusetts) Optima 4300DV spectrometer utilizing a Meinhard concentric glass nebulizer. Wavelengths of W that were analyzed were 207.912, 224.876, 239.708, and 248.923 nm and those for V were 290.880, 310.230, 309.310, and 292.402 nm. Samples were digested with a dilute 1% HF: HNO_3 (1:1) mixture for 5 min at 85 °C. Linear regression calibration was done with standards of varying W (0–15 ppm) and V (30–50 ppm) concentration. Standards were prepared by diluting commercial stock solutions of 1000 ppm W and V purchased from Inorganic Ventures.

SEM using an FEI Thermo Fisher (Hillsboro, Oregon) Apreo SEM at 25 kV accelerating voltage, 3.2 nA probe current, and 10.5561 mm working distance was performed to confirm particle size and morphology of unsubstituted and highly substituted samples produced *via* both microwave and furnace methods, as shown in Supplementary Fig. S4. Average grain size was estimated using the linear-intercept method and a correlation factor corresponding to a tetrakaidekahedron ($F_s = 1.775$) [70], and the analyzed micrographs can be seen in Supplementary Fig. S5. The synthesized powders do not have a consistent particle shape, but they can be said to be a mix of spherical and polyhedral shapes and the selected F_s was judged to be a good intermediate between the F_s of those shapes [70]. The line-intercept method is generally reserved for polished metallurgical micrographs but was used to give a rough estimate of the average grain size of the synthesized powders for comparison and is not

intended to provide an exhaustive quantitative value. In Supplementary Fig. S5(a), representative regions were selected for the analysis due to the preparation of the powders on the conductive tape leaving open spaces on the micrograph, which would lead to an overestimation in size of that sample. This was not necessary for the other micrographs. The mean intercept length and average grain size for each micrograph are presented in Supplementary Table S7.

DSC measurements were performed using a TA Instruments (New Castle, Delaware) Discovery DSC 2500 with a heating and cooling rate of 10 °C/min. SQUID measurements were performed using a Quantum Design (San Diego, California) MPMS3 to measure the metal-insulator transition temperature. A magnetic field of 70 kOe was applied while sweeping the temperature at a rate of 10 °C/min.

All PDF data were collected at a sample-to-detector distance of 175 mm with $\lambda = 0.24162$ Å. The least-squares refinement of the PDF data was accomplished using GSAS-II [69] for 2D powder pattern image integration, and fitting was performed using xPDFsuite [71]. For the integration, instrument parameters were obtained using a silicon standard, and the pin diode was masked out. A Kapton capillary background was subtracted from the $I(q)$ pattern individually for each sample. PDF parameters are as follows: $Q_{max\text{-}inst} = Q_{max} = 21.7$ Å^{-1}, $r_{poly} = 0.90$, $Q_{min} = 0.1$ Å^{-1}, $Q_{damp} = 0.0274$ Å^{-1}, and $Q_{broad} = 0.0086$ Å^{-1}. Q_{damp} and Q_{broad} were obtained through fitting a nickel standard. Parameters that were refined are as follows: (i) scale factor, (ii) lattice parameters, (iii) the quadratic correlation factor, and (iv) atomic displacement parameters U_{11}, U_{22}, U_{33}, and U_{13} where U_{12} and U_{23} are not symmetry allowed for either the monoclinic or tetragonal structures.

Acknowledgments

C.E.W., A.E.G., and V.D.N. acknowledge financial support from the Smart Vehicles Concepts Center, an NSF Industry–University Cooperative Research Center, (NSF IIP 1738723) for seed funding, The Ohio State University Institute for Materials Research Facility Grant (IMR-FG0213), and university funds. A.E.G. gratefully acknowledges the Advanced Undergraduate Researcher Award (AURA) and NexTech Materials, Ltd (Funding # 00058329) for financial support. Electron microscopy was performed at the Center for Electron Microscopy and Analysis (CEMAS) at the Ohio State University. ICP-OES was performed at the Trace Elements Research Laboratory (TERL) at the Ohio State University, with the help of TERL research associate Anthony Lutton. SQUID data were collected with the assistance of Phuong Tran and John Jamison. This research used resources of the Advanced Photon Source, a U.S. Department of Energy (DOE) Office of Science User Facility operated for the DOE Office of Science by Argonne National Laboratory under Contract No. DE-AC02-06CH11357. Research at the APS was conducted using general user proposals (GUP-61382 and GUP-62602). Part or all of the research described in this paper was performed at the Canadian Light Source, a national research facility of the University of Saskatchewan, which is supported by the Canada Foundation for Innovation (CFI), the Natural Sciences and Engineering Research Council (NSERC), the National Research Council (NRC), the Canadian Institutes of Health Research (CIHR), the Government of Saskatchewan, and the University of Saskatchewan. Research at CLS was conducted using general user proposal (RA-010714).

Supplementary Material

To view supplementary material for this article, please visit https://doi.org/10.1557/jmr.2020.250.

Author Contributions

C.E.W. collected synchrotron X-ray scattering data, performed the Rietveld and the PDF analyses, and collected and analyzed the SQUID data. A.E.G. developed the microwave synthesis heating methodology, prepared the samples, and collected synchrotron X-ray scattering data. J.J.A. contributed to sample preparations as well as collected and analyzed DSC data. P.A.L. collected and analyzed ICP-OES data. W.X. and G.K. were involved in the collection and analysis of the synchrotron XRD data. C.E.W., A.E.G., and V.D.N. wrote the manuscript. V.D.N. conceived of the original idea, supervised the findings of this work, and collected synchrotron X-ray scattering data. All authors discussed the results, provided critical feedback, and contributed to the final manuscript.

Conflict of Interest

The authors declare that there are no financial conflicts of interests.

References

1. **F.J. Morin**: Oxides which show a metal-to-insulator transition at the neel temperature. *Phys. Rev. Lett.* **3**, 34 (1959).
2. **C.N. Berglund and H.J. Guggenheim**: Electronic properties of VO_2 near the semiconductor-metal transition. *Phys. Rev.* **185**, 1022 (1969).
3. **J.B. Goodenough**: The two components of the crystallographic transition in VO_2. *J. Solid State Chem.* **3**, 490 (1971).
4. **D. Adler**: Mechanisms for metal-nonmental transitions in transition-metal oxides and sulfides. *Rev. Mod. Phys.* **40**, 714 (1968).
5. **N.F. Mott**: Metal-insulator transitions. *Pure Appl. Chem.* **52**, 65 (1980).

6. **N.F. Mott**: *Metal-Insulator Transitions*, 2nd ed. (Taylor & Francis Ltd, London, 1997).
7. **V. Eyert**: The metal-insulator transitions of VO_2: A band theoretical approach. *Ann. der Phys.* **11**, 650 (2002).
8. **R.M. Wentzcovitch, W.W. Schulz, and P.B. Allen**: VO_2: Peierls or Mott-Hubbard? A view from band theory. *Phys. Rev. Lett.* **72**, 3389 (1994).
9. **G. Andersson**. *Acta Chemica Scandinavica.* **10**, 623 (1956).
10. **A. Magnéli, G. Andersson, G. Sundkvist, and G. Sundkvist**. *Acta Chemica Scandinavica* **9**, 1378 (1955).
11. **D.B. McWhan, M. Marezio, J.P. Remeika, and P.D. Dernier**: X-ray diffraction study of metallic VO_2. *Phys. Rev. B* **10**, 490 (1974).
12. **S.A. Corr, D.P. Shoemaker, B.C. Melot, and R. Seshadri**: Real-space investigation of structural changes at the metal-insulator transition in VO_2. *Phys. Rev. Lett.* **105**, 1 (2010).
13. **W. Paul**: The present position of theory and experiment for VO_2. *Mater. Res. Bull.* **5**, 691 (1970).
14. **K.L. Holman, T.M. McQueen, A.J. Williams, T. Klimczuk, P.W. Stephens, H.W. Zandbergen, Q. Xu, F. Ronning, and R.J. Cava**: Insulator to correlated metal transition in $V_{1-x}Mo_xO_2$. *Phys. Rev. B—Condens. Matter Mater. Phys.* **79**, 1 (2009).
15. **A.S. Barker Jr, H.W. Verleur, and H.J. Guggenheim**: Infrared optical properties of vanadium dioxide above and below the transition temperature. *Phys. Rev. Lett.* **36**, 2137 (1976).
16. **C. Lamsal and N.M. Ravindra**: Optical properties of vanadium oxides—An analysis. *J. Mater. Sci.* **48**, 6341 (2013).
17. **M.M. Qazilbash, A.A. Schafgans, K.S. Burch, S.J. Yun, B.G. Chae, B.J. Kim, H.T. Kim, and D.N. Basov**: Electrodynamics of the vanadium oxides VO_2 and V_2O_3. *Phys. Rev. B—Condens. Matter Mater. Phys.* **77**, 1 (2008).
18. **K.C. Kam and A.K. Cheetham**: Thermochromic VO_2 nanorods and other vanadium oxides nanostructures. *Mater. Res. Bull.* **41**, 1015 (2006).
19. **W. Lv, D. Huang, Y. Chen, Q. Qiu, and Z. Luo**: Synthesis and characterization of Mo-W co-doped VO_2(R) nano-powders by microwave-assissted hydrothermal method. *Ceram. Int.* **40**, 12661 (2014).
20. **X. Tan, W. Liu, R. Long, X. Zhang, T. Yao, Q. Liu, Z. Sun, Y. Cao, and S. Wei**: Symmetry-controlled structural phase transition temperature in chromium-doped vanadium dioxide. *J. Phys. Chem. C* **120**, 28163 (2016).
21. **A. Zylbersztejn and N.F. Mott**: Metal-insulator transition in vanadium dioxide. *Phys. Rev. B* **11**, 4383 (1975).
22. **C. Sommers, R. De Groot, D. Kaplan, and A. Zylbersztejn**: Cluster calculations of the electronic d-states in VO_2. *J. Phys. Lett.* **36**, 157 (1975).
23. **J.B. Goodenough**: Direct cation–cation interactions. *Phys. Rev.* **117**, 1442 (1960).
24. **Z. Hiroi**: Structural instability of the rutile compounds and its relevance to the metal-insulator transition of VO_2. *Prog. Solid State Chem.* **43**, 47 (2015).
25. **X. Tan, T. Yao, R. Long, Z. Sun, Y. Feng, H. Cheng, X. Yuan, W. Zhang, Q. Liu, C. Wu, Y. Xie, and S. Wei**: Unraveling metal-insulator transition mechanism of VO_2 triggered by tungsten doping. *Sci. Rep.* **2**, 466 (2012).
26. **L. Whittaker, T.L. Wu, C.J. Patridge, G. Sambandamurthy, and S. Banerjee**: Distinctive finite size effects on the phase diagram and metal-insulator transitions of tungsten-doped vanadium(IV) oxide. *J. Mater. Chem.* **21**, 5580 (2011).
27. **M. Israelsson and L. Kihlborg**: The phase relations in the VO_2-WO_2 system. *J. Chem. Inf. Model.* **5**, 19 (1970).
28. **K. Shibuya, M. Kawasaki, and Y. Tokura**: Metal-insulator transition in epitaxial $V_{1-x}W_xO_2$ ($0 \leq x \leq 0.33$) thin films. *Appl. Phys. Lett.* **96**, 022102 (2010).
29. **M. Nygren and M. Israelsson**: A D.T.A. study of the semiconductor-metallic transition temperature in $V_{1-x}W_xO_2$, $0 \leq x \leq 0.067$. *Mater. Res. Bull.* **4**, 881 (1969).
30. **S.A. Lawton and E.A. Theby**: Effect of tungsten and molybdenum doping on the semiconductor-metallic transition in vanadium dioxide produced by evaporative decomposition of solutions and hydrogen reduction. *J. Am. Ceram. Soc.* **78**, 238 (1995).
31. **J.P. Pouget, H. Launois, J.P. D'Haenens, P. Merenda, and T.M. Rice**: Electron localization induced by uniaxial stress in pure VO_2. *J. Chem. Inf. Model.* **53**, 1689 (2012).
32. **S. Chen, X. Zhang, Q. Zhang, and W. Tan**: Trioctylphosphine as both solvent and stabilizer to synthesize CdS nanorods. *Nanoscale Res. Lett.* **4**, 1159 (2009).
33. **K. Kosuge**: The phase transition in VO_2. *J. Phys. Soc. Japan* **22**, 551 (1967).
34. **G. Villeneuve, A. Bordet, A. Casalot, J.P. Pouget, H. Launois, and P. Lederer**: Contribution to the study of the metal-insulator transition in the $V_{1-x}Nb_xO_2$ system: I—crystallographic and transport properties. *J. Phys. Chem. Solids* **33**, 1953 (1972).
35. **Z. Yang, C. Ko, and S. Ramanathan**: Oxide electronics utilizing ultrafast metal-insulator transitions. *Annu. Rev. Mater. Res.* **41**, 337 (2011).
36. **J. Nag and R.F. Haglund**: Synthesis of vanadium dioxide thin films and nanoparticles. *J. Phys. Condens. Matter* **20**, 264016 (2008).
37. **K. Muramoto, Y. Takahashi, N. Terakado, Y. Yamazaki, S. Suzuki, and T. Fujiwara**: VO_2-dispersed glass: A new class of phase change material. *Sci. Rep.* **8**, 1 (2018).
38. **M.M. Qazilbash, M. Brehm, B.-G. Chae, P.-C. Ho, G.O. Andreev, B.-J. Kim, S.J. Yun, A.V. Balatsky, M.B. Maple, F. Keilmann, H.-T. Kim, and D.N. Basov**: Mott transition in VO_2 revealed by infrared spectroscopy and nano-imaging. *Science* **318**, 1750 (2007).

39. **B.G. Chae, H.T. Kim, S.J. Yun, B.J. Kim, Y.W. Lee, D.H. Youn, and K.Y. Kang**: Highly oriented VO_2 thin films prepared by sol-gel deposition. *Electrochem. Solid-State Lett.* **9**, C12 (2006).
40. **S.A. Corr, M. Grossman, J.D. Furman, B.C. Melot, A.K. Cheetham, K.R. Heier, and R. Seshadri**: Controlled reduction of vanadium oxide nanoscrolls: Crystal structure, morphology, and electrical properties. *Chem. Mater.* **20**, 6396 (2008).
41. **T.E. Ashton, D. Hevia Borrás, A. Iadecola, K.M. Wiaderek, P.J. Chupas, K.W. Chapman, and S.A. Corr**: Microwave-assisted synthesis and electrochemical evaluation of VO_2 (B) nanostructures. *Acta Crystallogr. Sect. B Struct. Sci. Cryst. Eng. Mater.* **71**, 722 (2015).
42. **J. Pan, L. Zhong, M. Li, Y. Luo, and G. Li**: Microwave-assisted solvothermal synthesis of VO_2 hollow spheres and their conversion into V_2O_5 hollow spheres with improved lithium storage capability. *Chem.—Eur. J.* **22**, 1461 (2016).
43. **A.J. Littlejohn, Y. Yang, Z. Lu, E. Shin, K.C. Pan, G. Subramanyam, V. Vasilyev, K. Leedy, T. Quach, T.M. Lu, and G.C. Wang**: Naturally formed ultrathin V_2O_5 heteroepitaxial layer on VO_2 /sapphire(001) film. *Appl. Surf. Sci.* **419**, 365 (2017).
44. **M.B. Sahana, M.S. Dharmaprakash, and S.A. Shivashankar**: Microstructure and properties of VO_2 thin films deposited by MOCVD from vanadyl acetylacetonate. *J. Mater. Chem.* **12**, 333 (2002).
45. **L. Chen, M. Fiore, J.E. Wang, R. Ruffo, D.-K. Kim, and G. Longoni**: Readiness level of sodium-ion battery technology: A materials review. *Adv. Sustain. Syst.* **2**, 1700153 (2018).
46. **C. Wang, W. Ping, Q. Bai, H. Cui, R. Hensleigh, R. Wang, A.H. Brozena, Z. Xu, J. Dai, Y. Pei, C. Zheng, G. Pastel, J. Gao, X. Wang, H. Wang, J. Zhao, B. Yang, J. Luo, Y. Mo, B. Dunn, and L. Hu**: A general method to synthesize and sinter bulk ceramics in seconds. *Science* **368**, 521 (2020).
47. **C. Zhang, X. Wang, Q. Liang, X. Liu, Q. Weng, J. Liu, Y. Yang, Z. Dai, K. Ding, Y. Bando, J. Tang, and D. Golberg**: Amorphous phosphorus/nitrogen-doped graphene paper for ultrastable sodium-ion batteries. *Nano Lett.* **16**, 2054 (2016).
48. **J.H. Grebenkemper, J.D. Bocarsly, E.E. Levin, G. Seward, C. Heikes, C. Brown, S. Misra, F. Seeler, K. Schierle-Arndt, S.D. Wilson, and R. Seshadri**: Rapid microwave preparation and composition tuning of the high-performance magnetocalorics $(Mn,Fe)_2(P,Si)$. *ACS Appl. Mater. Interfaces* **10**, 7208 (2018).
49. **A.R. Siamaki, A.E.R.S. Khder, V. Abdelsayed, M.S. El-Shall, and B.F. Gupton**: Microwave-assisted synthesis of palladium nanoparticles supported on graphene: A highly active and recyclable catalyst for carbon-carbon cross-coupling reactions. *J. Catal.* **279**, 1 (2011).
50. **S.L. Pedersen, A.P. Tofteng, L. Malik, and K.J. Jensen**: Microwave heating in solid-phase peptide synthesis. *Chem. Soc. Rev.* **41**, 1826 (2012).
51. **R. Behrendt, P. White, and J. Offer**: Advances in Fmoc solid-phase peptide synthesis. *J. Pept. Sci.* **22**, 4 (2016).
52. **M.H. Bhat, A. Miura, P. Vinatier, A. Levasseur, and K.J. Rao**: Microwave synthesis of lithium lanthanum titanate. *Solid State Commun.* **125**, 557 (2003).
53. **J. Guo, C. Dong, L. Yang, and G. Fu**: A green route for microwave synthesis of sodium tungsten bronzes Na_xWO_3 ($0<x<1$). *J. Solid State Chem.* **178**, 58 (2005).
54. **M. Iwasaki, H. Takizawa, K. Uheda, T. Endo, and M. Shimada**: Microwave synthesis of LaCrO. *J. Mater. Chem.* **8**, 2765 (1998).
55. **Y.F. Liu, X.Q. Liu, and G.Y. Meng**: A novel route of synthesizing $La_{1-x}Sr_xCoO_3$ by microwave irradiation. *Mater. Lett.* **48**, 176 (2001).
56. **S.W. Muir, O.D. Rachdi, and M.A. Subramanian**: Rapid microwave synthesis of the iron arsenides NdFeAsO and $NdF_{0.9}Co_{0.1}AsO$. *Mater. Res. Bull.* **47**, 798 (2012).
57. **K.J. Rao, P.A. Ramakrishnan, and R. Gadagkar**: Microwave preparation of oxide bronzes. *J. Solid State Chem.* **148**, 100 (1999).
58. **S. Saremi-Yarahmadi, B. Vaidhyanathan, and K.G.U. Wijayantha**: Microwave-assisted low temperature fabrication of nanostructured α-Fe_2O_3 electrodes for solar-driven hydrogen generation. *Int. J. Hydrogen Energy* **35**, 10155 (2010).
59. **H.J. Kitchen, S.R. Vallance, J.L. Kennedy, N. Tapia-Ruiz, L. Carassiti, A. Harrison, A.G. Whittaker, T.D. Drysdale, S.W. Kingman, and D.H. Gregory**: Modern microwave methods in solid-state inorganic materials chemistry: From fundamentals to manufacturing. *Chem. Rev.* **114**, 1170 (2014).
60. **E.E. Levin, J.H. Grebenkemper, T.M. Pollock, and R. Seshadri**: Protocols for high temperature assisted-microwave preparation of inorganic compounds. *Chem. Mater.* **31**, 7151 (2019).
61. **A.C. Metaxas and R.J. Meredith**: *Industrial Microwave Heating*, 1st ed. (The Institute of Engineering and Technology, London, 1989), pp. 1–36.
62. **Z. Peng, J.Y. Hwang, J. Mouris, R. Hutcheon, and X. Huang**: Microwave penetration depth in materials with non-zero magnetic susceptibility. *ISIJ Int.* **50**, 1590 (2010).
63. **N. Emond, A. Hendaoui, S. Delprat, M. Chaker, and K. Wu**: Theoretical and experimental investigation of thermo-tunable metal-insulator-vanadium dioxide coplanar waveguide structure. *IEEE Trans. Microw. Theory Tech.* **65**, 1443 (2017).
64. **F. Predel**: *Phase Equilibria, Crystallographic and Thermodynamic Data of Binary Alloys* (Springer-Verlag, **Vol. 12D**, Berlin, 2016).
65. **R.D. Shannon and C.T. Prewitt**: Effective ionic radii in oxides and fluorides. *Acta Crystallogr. Sect. B Struct. Crystallogr. Cryst. Chem.* **25**, 925 (1969).
66. **T. Egami and S.J.L. Billinge**: *Underneath the Bragg Peaks: Structural Analysis of Complex Materials*, 1st ed. (Elsevier, Oxford, 2003).
67. **C. Tang, P. Georgopoulos, M.E. Fine, J.B. Cohen, M. Nygren, G.S. Knapp, and A. Aldred**: Local atomic and electronic arrangements in $W_xV_{1-x}O_2$. *Phys. Rev. B* **31**, 1000 (1985).
68. **E.J. Braham, D. Sellers, E. Emmons, R. Villarreal, H. Asayesh-Ardakani, N.A. Fleer, K.E. Farley,**

R. Shahbazian-Yassar, R. Arròyave, P.J. Shamberger, and S. Banerjee: Modulating the hysteresis of an electronic transition: Launching alternative transformation pathways in the metal-insulator transition of vanadium(IV) oxide. *Chem. Mater.* **30**, 214 (2018).

69. **B.H. Toby and R.B. Von Dreele**: GSAS-II: The genesis of a modern open-source all purpose crystallography software package. *J. Appl. Crystallogr.* **46**, 544 (2013).
70. **J.-H. Han and D.-Y. Kim**: Analysis of the proportionality constant correlating the mean intercept length to the average grain size. *Acta Met. Mater.* **43**, 3185 (1995).
71. **P. Juhás, C.L. Farrow, X. Yang, K.R. Knox, and S.J.L. Billinge**: Complex modeling: A strategy and software program for combining multiple information sources to solve ill posed structure and nanostructure inverse problems. *Acta Crystallogr. Sect. A Found. Adv.* **71**, 562 (2015).